

See discussions, stats, and author profiles for this publication at: <https://www.researchgate.net/publication/263389780>

Oxygen Reduction Contributing to Charge Transfer during the First Discharge of the CeO₂–Bi₂Fe₄O₉–Li Battery: In Situ X-ray Diffraction and X-ray Absorption Near-Edge Structure Inve...

ARTICLE *in* THE JOURNAL OF PHYSICAL CHEMISTRY C · JUNE 2014

Impact Factor: 4.77 · DOI: 10.1021/jp4105689

CITATION

1

READS

78

9 AUTHORS, INCLUDING:



Min Liu

Shanghai Institute of Applied Physics

7 PUBLICATIONS 17 CITATIONS

[SEE PROFILE](#)



Yueliang Gu

Shanghai Institute of Applied Physics

4 PUBLICATIONS 22 CITATIONS

[SEE PROFILE](#)



Tieying Yang

Shanghai Institute of Applied Physics

24 PUBLICATIONS 112 CITATIONS

[SEE PROFILE](#)



Wen Wen

49 PUBLICATIONS 995 CITATIONS

[SEE PROFILE](#)

Oxygen Reduction Contributing to Charge Transfer during the First Discharge of the $\text{CeO}_2\text{--Bi}_2\text{Fe}_4\text{O}_9\text{--Li}$ Battery: In Situ X-ray Diffraction and X-ray Absorption Near-Edge Structure Investigation

Min Liu,[†] Chuan Lin,[‡] Yueliang Gu,[§] Tieying Yang,[§] Zhengliang Gong,^{||} Guangzhi Yin,[§] Xingyu Gao,[§] Xingtai Zhou,[†] and Wen Wen^{*§}

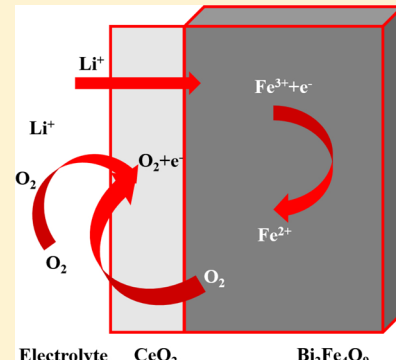
[†]Key Laboratory of Nuclear Radiation and Nuclear Energy Technology, Shanghai Institute of Applied Physics, Chinese Academy of Sciences, 2019 Jialuo Road, Shanghai 201800, P. R. China

[‡]Materials Characterization Lab., General Electric Global Research Center-Shanghai, Zhangjiang High-Tech. Park, Pudong New Area, Shanghai 201203, P. R. China

[§]Shanghai Synchrotron Radiation Facility, Shanghai Institute of Applied Physics, Chinese Academy of Sciences, Zhangjiang High-Tech. Park, Pudong New Area, Shanghai 201204, P. R. China

^{||}College of Energy, Xiamen University, Xiamen 361005, P. R. China

ABSTRACT: Since pioneering work performed by Rouxel et al. that emphasizes the effects of anions in the ionic intercalation process, the role of oxygen ions in lithium ionic battery electrodes is of great interest since it will give new directions to further enhance the battery capacity. In this paper, $\text{Bi}_2\text{Fe}_4\text{O}_9\text{--CeO}_2$ was synthesized and was used as an anode for second lithium batteries application. A large amount of oxygen vacancies exist in both CeO_2 and $\text{Bi}_2\text{Fe}_4\text{O}_9$. In CeO_2 , oxygen vacancies are mainly located at the 111 plane, and in $\text{Bi}_2\text{Fe}_4\text{O}_9$, oxygen vacancies are mainly located at the 002 plane. Li^+ insertion into $\text{Bi}_2\text{Fe}_4\text{O}_9$ produced high spin tetrahedral Fe^{2+} , which is Jahn–Teller active and induces shrinkage of the $\text{Bi}_2\text{Fe}_4\text{O}_9$ lattice and releases O_2 . The released O_2 is further reduced and contributes to ~ 70 mAh/g during the first discharge process. The 002 plane of $\text{Bi}_2\text{Fe}_4\text{O}_9$ is very reactive for oxygen reduction, where there are not only a lot of oxygen vacancies but also tetrahedral Fe^{3+} ions participating in producing more oxygen vacancies. This work gives new directions for future design of lithium battery electrodes, which can reversibly evolve/reduce O_2 , and the O_2/O^{2-} (or O^-) redox couple is responsible for charge transfer.



1. INTRODUCTION

Lithium ion batteries have wide applications in portable electronics, and there are increasing demands for longer cycling life, better discharge energy density, and larger volumetric density, etc., especially with their potential application in electric vehicles.¹ In a typical lithium ion battery, Li ions were inserted into/extracted out of the electrodes with concomitant reduction/oxidation of certain elements to balance the charge.

Usually, cationic redox couples such as $\text{Co}^{4+}/\text{Co}^{3+}$ in LiCoO_2 , $\text{Mn}^{4+}/\text{Mn}^{3+}$ in LiMn_2O_4 , and $\text{Fe}^{3+}/\text{Fe}^{2+}$ in LiFePO_4 can be responsible for charge balance. However, as pointed out by Rouxel et al.,^{2,3} hybridization of cationic and anionic molecular orbitals in a transition metal oxide might involve both cations and anions for charge balance during the ionic intercalation process. There naturally are a lot of concerns about anionic redox couples, such as O^{2-}/O^- , because oxygen might also contribute to charge transfer in some materials, such as Zn-doped LiMn_2O_4 ,⁴ $\text{LiNi}_{0.8}\text{Co}_{0.2}\text{O}_2$,⁵ LiCoO_2 ,⁶ $\text{LiMn}_{1/3}\text{Ni}_{1/3}\text{Co}_{1/3}\text{O}_2$,⁷ etc. In Zn-doped LiMn_2O_4 , the O^{2-}/O^- redox couple is the origin for the 5 V activity.⁴ In LiCoO_2 , O^{2-} ions could play a significant role to balance the charge.⁶ In $\text{LiMn}_{1/3}\text{Ni}_{1/3}\text{Co}_{1/3}\text{O}_2$, O^{2-} ions can be functionalized⁷ (as an

electron donor at the end of the charge step). Some surface coatings with excellent oxygen ionic conductor, such as ZrO_2 ^{8,9} or CeO_2 ^{10,11} can enhance the electrochemical performance of LiCoO_2 , $\text{LiCo}_{0.2}\text{Mn}_{0.8}\text{O}_2$,¹⁰ and $\text{LiCo}_{1/3}\text{Mn}_{1/3}\text{Ni}_{1/3}\text{O}_2$.¹¹ Recently, there are some reports on the role of oxygen during the electrochemical cycling process of $\text{Li}_{1.20}\text{Mn}_{0.54}\text{Co}_{0.13}\text{Ni}_{0.13}\text{O}_2$,^{12,13} and they proposed that extra capacity during the first charge is due to surface O^{2-} evolving out of the crystal lattice (to form O_2). The lattice O^{2-}/O^- reversible redox couple is partly responsible for charge balance. Another series of work performed by Tarascon et al. proposed the reversible O^{2-}/O^- transformation in Ru-doped Li_2MnO_3 .^{14,15}

To further investigate how lattice O^{2-} is involved in the electrochemical process, bismuth oxides, which could have excellent oxygen ionic conductivity,^{16,17} were employed as electrodes. Recently, few works have been carried out on bismuth ferrate batteries.^{18–20} After discharging to 0.05 V,

Received: October 25, 2013

Revised: June 13, 2014

Published: June 13, 2014

BiFeO_3 could have a discharge capacity more than 1000 mAh/g. A three-step three-electron transfer of Bi(III) to Bi(0) was observed during the electrochemical discharge process.¹⁹ It is also clearly observed that there are two transportation pathways for both ionic and electronic transportations.²⁰ Combining in situ X-ray diffraction and absorption techniques, the detailed discharge mechanism was clearly elucidated.

$\text{Bi}_2\text{Fe}_4\text{O}_9$ is a good O^{2-} ionic conductor.²¹ Its crystal structure, which is displayed in Figure 1, has been discussed in

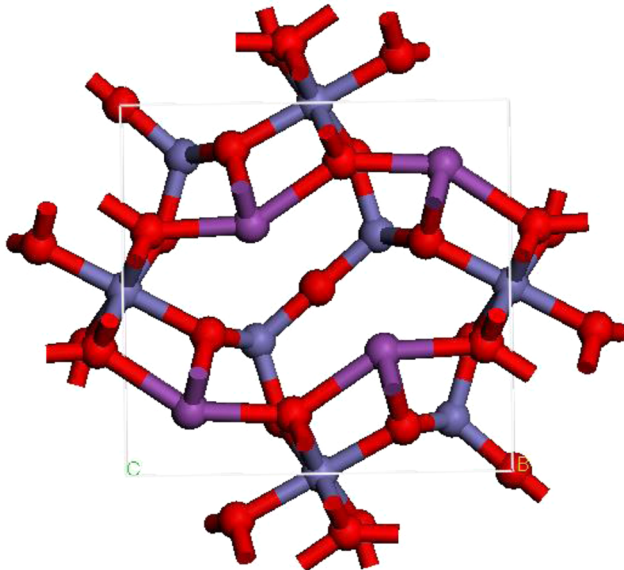


Figure 1. Ball–stick model of $\text{Bi}_2\text{Fe}_4\text{O}_9$ viewed along the c axis. Oxygen ions, red; iron ions, blue; bismuth ions, purple.

detail in the literature.^{22–25} In the orthorhombic unit cell, Bi ions are aligned along the c axis direction, and there are two coordination environments for Fe ions, edge-sharing FeO_6 octahedrons along the c axis and vertex-sharing Fe_2O_7 tetrahedrons along a and b axes.^{22–25} In this work, the $\text{CeO}_2-\text{Bi}_2\text{Fe}_4\text{O}_9$ composite was synthesized, and its electrochemical property was evaluated. Combined in situ X-ray diffraction and absorption spectroscopy were employed to study the discharge mechanism. CeO_2 was added not only as an oxygen donor/acceptor, which might be critical for ionic transports of $\text{Bi}_2\text{Fe}_4\text{O}_9$, but also as a coating for better electrochemical contact.

2. MATERIALS SYNTHESIS AND CHARACTERIZATION

2.1. Materials Synthesis. The materials with different Ce amount were synthesized using a coprecipitation route similar to that reported earlier.^{19,20} For a typical synthesis, a stoichiometric amount of $\text{Fe}(\text{NO}_3)_3 \cdot 9\text{H}_2\text{O}$, $\text{Bi}(\text{NO}_3)_3 \cdot 5\text{H}_2\text{O}$, and $\text{Ce}(\text{NO}_3)_3 \cdot 5\text{H}_2\text{O}$ was dissolved in deionized water. A small amount of dilute nitric acid was added to help the dissolution process. $\text{NH}_3 \cdot \text{H}_2\text{O}$ was then dropwise added into the solution to precipitate cationic ions, until the pH of the solution is adjusted to ~ 10 . In other words, all the cationic ions were successfully deposited. The water was evaporated, and the remaining solid was heated at 250°C for 1 h to get rid of NO_3^- and NH_3 . The sample then was heat-treated at a ramping rate of $2^\circ\text{C}/\text{min}$ to a required temperature and held for 0.5 h.

2.2. Ex Situ XRD Characterization. Ex situ XRD was performed at BL14B1 of the Shanghai Synchrotron Radiation

Facility (SSRF) at a wavelength of 1.2398 \AA .^{19,20} A Bede scintillation point detector was employed for data collection in flat plate mode. The step size used was 0.02° . BL14B1 is a bending magnet beamline and uses a Si(111) double-crystal monochromator for energy selection. The typical focused beam size is $\sim 0.5 \text{ mm} \times 0.5 \text{ mm}$. Ex situ XRD patterns were viewed and analyzed using the CMPLR program.²⁶ An EXPGUI code was used for XRD profile fitting.^{27–29}

2.3. Transmission Electron Microscopy Measurements. The transmission electron microscopy (TEM) measurements were performed using an FEI Tecnai G2 F20 S-TWIN TEM. The samples were at first painted in a graphite film (Cu grid) and then transferred into the vacuum chamber.

2.4. Electrochemical Galvanostatic Cyclings. The electrochemical galvanostatic cyclings were performed similar to those reported before,^{19,20} and metallic Li foil was used as an anode. For a standard procedure, 150 mg of active material, 25 mg of polyvinyl difluoride, and 25 mg of acetylene black were mixed homogeneously, and some *N*-methyl-2-pyrrolidone (NMP) was added to the mixture to make the paste. The resulted slurry was manually painted into a thin Cu foil (0.01 mm) in the size of $30 \text{ mm} \times 30 \text{ mm}$. The Cu foil (with sample) was transferred to a vacuum oven at 120°C for 2 h to remove the NMP residue (in vacuum). The dried sample was then used for battery assembling. Unless specified, the current density used for the electrochemical galvanostatic cycling was $\sim 20 \text{ mA/g}$. Cu foil (thickness of 0.1 mm) was used for current collectors at both anode and cathode sides.

2.5. XANES Studies. **2.5.1. Ex Situ Fe K-Edge.** Ex situ Fe K-edge X-ray absorption near-edge structure (XANES) spectra were obtained at BL14W1 of the Shanghai Synchrotron Radiation Facility using transmission mode.^{30–32} This beamline is wiggler based, and the Si(111) double crystal was employed to tune the energy. A Toroidal mirror was employed to focus the beam into a size of $0.5 \text{ mm} \times 0.5 \text{ mm}$. Fe foil was used for energy calibration. For the Fe K-edge, gas used for the I_0 chamber is 5% N_2 /95% He, and that for I_t chamber is 50% N_2 /50% Ar, respectively. Standard XANES spectra of FeO , Fe_2O_3 , and Fe_3O_4 were collected for comparison. Two batteries that are in different stages of the discharge process were studied. The first battery is freshly assembled, and the second one is fully discharged using a discharge current density of $\sim 20 \text{ mA/g}$. These two batteries were assembled using the spectroelectrochemical cell, which has been discussed in detail elsewhere.^{33–35} It has a Mylar window at both the cathode and anode sides and allows the X-ray to penetrate through for accurate measurements. In this configuration, both current collectors in the anode and cathode sides have a small window of $2 \text{ mm} \times 2 \text{ mm}$ cut for the beam path. The Athena module of IFEFFIT was used for E_0 selection, background subtraction, and normalization.³⁶ The typical time for one scan is about 14 minutes. A typical XANES scan is collected using five segments. The pre-edge region is collected from -100 to -20 eV with a step size of 5 eV. Near the edge region, the data are collected from -20 to 50 eV with a step size of 0.5 eV. After the edge, the data are further collected between 50 – 100 eV , 100 – 300 eV , and 300 – 500 eV with step sizes of 1, 2, and 5 eV. For all five segments, the integration time is 1 s.

2.5.2. Ex Situ Bi L_{III} -Edge. For the Bi L_{III} -edge XANES spectrum, a Pb foil was used for energy calibration. The XANES spectrum of Bi_2O_3 was collected for comparison. The gas used for the I_0 chamber is 100% N_2 , and the gas used for the transmission chamber (I_t) is 100% Ar.

2.5.3. In Situ Fe K-Edge. For in situ experiments, a spectroelectrochemical cell was employed for data collection. Also for the in situ experiments, the active material was peeled off from the thin Cu foil for a better signal. To catch changes in situ, a smaller discharge current density of ~ 5 mA/g was used before 74.1 mAh/g. The in situ battery was stopped at 74.1 mAh/g and further was measured using the Bi L_{III}-edge right after Fe K-edge XANES measurements.

2.5.4. In Situ Bi L_{III}-Edge. For in situ experiments, a spectroelectrochemical cell was employed for data collection. The current density used is ~ 90 mA/g. Also for the in situ experiments, active material was peeled off from the thin Cu foil for a better signal.

2.6. In Situ XRD. The in situ XRD experiments were carried out at beamline BL14B1 of the Shanghai Synchrotron Radiation Facility at a wavelength of 1.2398 Å.^{19,20} A spectroelectrochemical cell feature was employed for in situ XRD experiments. A MAR225 CCD detector was employed for data collection, and a fit2d code was used for data integration. La₆ was used for the energy calibration. The typical time for one scan is 120 s. During in situ XRD experiments, the electrochemical discharge is carried out using two different current densities. Before ~ 140 mAh/g, it was discharged using a current density of ~ 20 mA/g to probe minor changes induced by Li⁺ ion insertion. After that it was discharged with a current density of ~ 90 mA/g.

2.7. XRD Data Profile Fitting. XRD data were fitted with the combination of Gaussian and Lorenzian profiles using an EXPGUI code.^{27–29}

3. RESULTS AND DISCUSSION

3.1. Characterization of the Synthesized Material.

Figure 2a displays the X-ray diffraction patterns of the synthesized samples. When 20% CeO₂ was added, a significant amount of BiFeO₃ was produced at 700 °C. When 30% CeO₂ was added, the major phase is Bi₂Fe₄O₉, while minor BiFeO₃ can still be observed at 670 °C. The BiFeO₃ phase disappeared after the synthesis temperature was further increased to 700 °C. Actually this compound can be profile-fitted with two compositions of Bi₂Fe₄O₉ and CeO₂. Typical profile fitting results were displayed in Figure 2b. The refined data are consistent with an orthorhombic crystal structure with *pbam* space group, and the unit cell parameters are $a = 7.9694$ Å, $b = 8.4685$ Å, and $c = 6.0207$ Å. The lattice parameter of CeO₂ is refined to 5.4728 Å, which is slightly larger compared with the reported value of 5.411 Å³⁷ and indicates that there are some oxygen vacancies in the synthesized compound.

Figures 3a and 3b are TEM images of 30% Ce-coated Bi₂Fe₄O₉ synthesized at 700 °C. In Figure 3a, two kinds of particles can be clearly resolved with sizes ~ 5 and 15 nm, respectively. Their corresponding *d* spacing values are 3.16 and 3.18 Å and can be indexed to CeO₂(111) and Bi₂Fe₄O₉(121) planes, respectively. There are a large amount of oxygen vacancies at the interface of these two crystal planes which indicate that there are some interfacial interactions between particles of CeO₂ and Bi₂Fe₄O₉. The similarity of lattice spacing might be the reason for the interfacial interactions. Oxygen vacancies observed in CeO₂ are consistent with its lattice parameter refinement.

Figure 3b displays a single Bi₂Fe₄O₉ particle, and the surface facets can be clearly observed. The highlighted area is the (002) direction of Bi₂Fe₄O₉ with *d* spacing ~ 3.02 Å, which actually bisects two Fe octahedrons (edge sharing) along the *c* axis, and

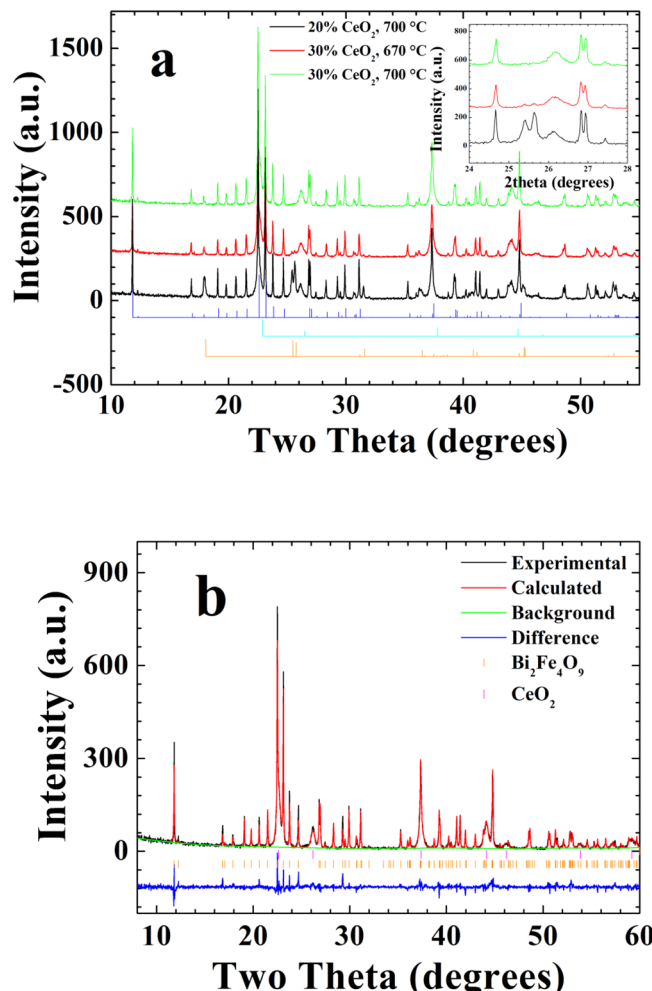


Figure 2. (a) XRD patterns of CeO₂ added Bi₂Fe₄O₉ synthesized at 670 °C (red, 30% CeO₂) and 700 °C (black, 20% CeO₂; green, 30% CeO₂). Diffraction patterns of standard Bi₂Fe₄O₉ (blue), CeO₂ (light blue), and BiFeO₃ (orange) were displayed at the bottom. (b) Typical fitting results using an EXPGUI code. Black, experimental; red, calculated; green, background; blue, difference from experimental and calculated data. The sample is 30% CeO₂ added Bi₂Fe₄O₉ synthesized at 700 °C.

the surface is dominated by O²⁻ ions. There are a significant amount of oxygen vacancies in (002), as highlighted in the figure. After loss of surface oxygen ions, the subsurface is exposed, and the one-dimensional channels along the *c* axis, where Bi ions are located, are clearly displayed.

3.2. Galvanostatic Electrochemical Cycling of the Bi₂Fe₄O₉–CeO₂–Li Battery. Figure 4 displays typical electrochemical cycling profiles of the CeO₂–Bi₂Fe₄O₉ composite with two different discharge current densities: ~ 20 and 90 mA/g. Similar to discharge of BiFeO₃,^{19,20} Bi₂Fe₄O₉ also displays good capability for Li intercalation. Using a cutoff voltage of 0.05 V, the first discharge capacity is ~ 700 mAh/g. The electrochemical discharge can be observed in four regions, which are highlighted in Figure 4a. This includes the first region located at ~ 1.2 V with a discharge capacity of ~ 70 mAh/g, which is about a two-electron transfer process if calculated according to the formula of $Q = NF/M$, where Q is the theoretical discharge capacity, N the number of electrons transferred, F the Faraday constant, and M the molecular weight (for Bi₂Fe₄O₉, $M = 785.331$ g/mol). In this region, there

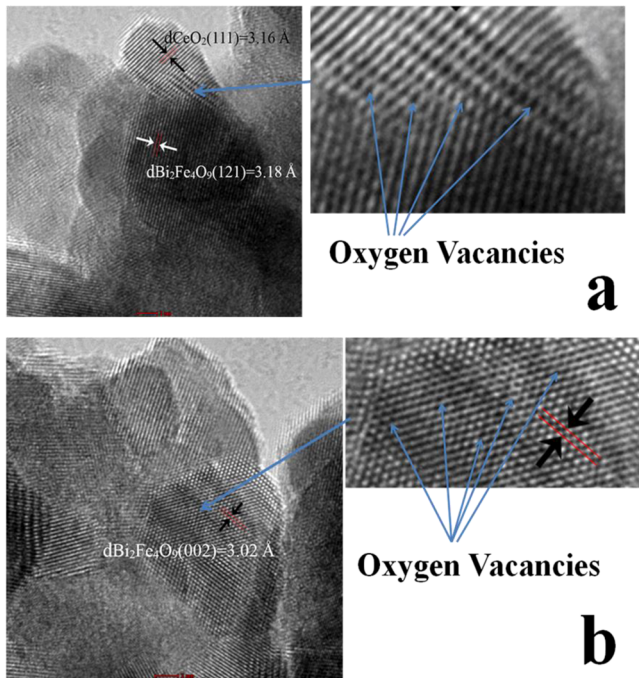


Figure 3. High-resolution TEM images of 30% Ce added $\text{Bi}_2\text{Fe}_4\text{O}_9$ synthesized at $700\text{ }^\circ\text{C}$: (a) $\text{CeO}_2(111)$ ($d = 3.16\text{ \AA}$) and $\text{Bi}_2\text{Fe}_4\text{O}_9(121)$ ($d = 3.18\text{ \AA}$). Zoomed image is to highlight the oxygen vacancies at the interface between particles of CeO_2 and $\text{Bi}_2\text{Fe}_4\text{O}_9$, (b) $\text{Bi}_2\text{Fe}_4\text{O}_9(002)$ ($d = 3.02\text{ \AA}$). Zoomed image is to highlight the oxygen vacancies.

is a voltage increase observed between ~ 15 to $\sim 35\text{ mAh/g}$. Between 70 to $\sim 200\text{ mAh/g}$ (second region), the cell voltage gradually decreased to $\sim 0.9\text{ V}$ and corresponds to a ~ 4 -electron transfer process. Between 200 to $\sim 460\text{ mAh/g}$ (third region), the cell voltage almost stabilized at $\sim 0.9\text{ V}$ and displayed a different trend of cell voltage decrease. This is consistent with about 7-electron transfer. When the capacity was more than 460 mAh/g (fourth region), the cell voltage displayed a relatively larger trend of decrease until 0.05 V . When the CeO_2 – $\text{Bi}_2\text{Fe}_4\text{O}_9$ battery discharged at a current density of $\sim 90\text{ mA/g}$, a similar discharge profile could be observed compared with that when it was discharged at $\sim 20\text{ mA/g}$, except that cell voltage is only slightly lower, especially at the second discharge, indicating that this compound can sustain large current density. The first two discharge capacities of ~ 700 and $\sim 400\text{ mAh/g}$ are also comparable with those discharged at 20 mA/g , while the voltage is slightly decreased at higher current density. In the second discharge, the battery can be discharged at relatively higher voltage, similar to what is observed in the discharge of other transition metal oxides, such as MnO , CoO , and NiO , etc.^{38,39}

A zoomed view of the voltage increase observed in Figure 4a is displayed in the Figure 4b inset. It is surprising since usually the cell voltage is expected to decrease during the discharge process, as observed in LiCoO_2 , LiMn_2O_4 , and LiFePO_4 . Sometimes, as displayed in Figure 4b, during the discharge process, the cell voltage may first decrease rapidly below 1 V and then gradually increase back to the discharge profile similar to those observed in Figure 4a. The voltage profile could even display two dips during discharge.

The voltage profile observed in Figure 4 seems unusual, and it could be the result of a phase transition. Thus, *in situ* XANES

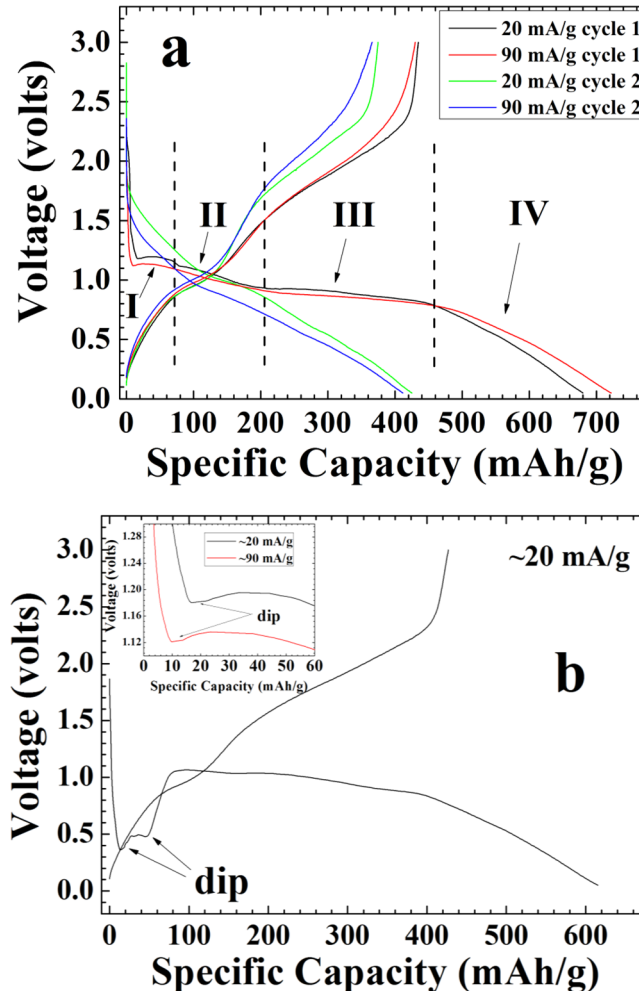


Figure 4. (a) Galvanostatic cycling profiles of $\text{Bi}_2\text{Fe}_4\text{O}_9$ – CeO_2 /Li batteries using different discharge current densities. Comparison of electrochemical cycling profiles of $\text{Bi}_2\text{Fe}_4\text{O}_9$ – CeO_2 /Li batteries. Black, 20 mA/g , cycle 1; red, 90 mA/g , cycle 1; green, 20 mA/g , cycle 2; blue, 90 mA/g , cycle 2. (b) The galvanostatic cycling profiles of $\text{Bi}_2\text{Fe}_4\text{O}_9$ – CeO_2 /Li batteries using a current density of $\sim 20\text{ mA/g}$, where the first discharge displays a large voltage drop below 0.5 V and two dips could be observed. Inset is the zoomed view of (a), where a voltage increase was observed.

and XRD studies were performed to study both electronic and structural changes, such as oxidation state changes, lattice parameter changes, etc., of the active materials during the electrochemical cycling process.

3.3. Study of Cations' Oxidation State Change Using XANES. **3.3.1. Ex Situ Fe K-Edge XANES Measurements.** Figure 5a displayed ex situ Fe K-edge X-ray absorption spectroscopy spectra of a freshly assembled battery and fully discharged one. A few standard compounds of Fe_2O_3 , Fe_3O_4 , and FeO were also displayed for comparison. The absorption edge position of FeO , Fe_3O_4 , and Fe_2O_3 displayed regular edge shifts, which in return are highly consistent with their oxidation states. The pre-edge feature is often used to characterize the coordination environment of the transition metals. It is a $1s$ to $3d$ dipole forbidden transition, while it could be quadrupole allowed due to orbital hybridization.^{40,41} As can be clearly observed in the pre-edge region of Fe_2O_3 and Fe_3O_4 , the symmetric 6-coordinated FeO_6 in Fe_2O_3 displayed smaller intensity compared with that of Fe_3O_4 , where $1/3$ of Fe ions are

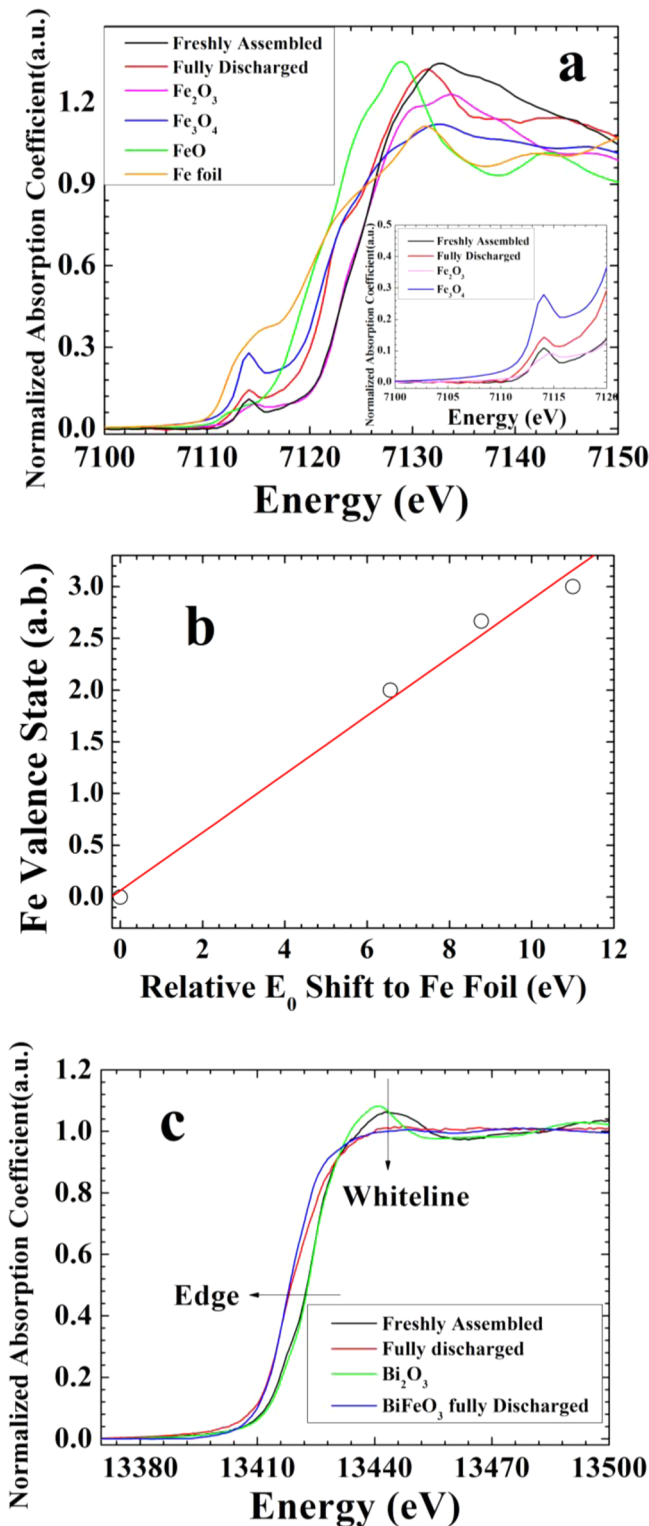


Figure 5. (a) Ex situ Fe K-edge X-ray absorption spectroscopy spectra of the freshly assembled battery and the fully discharged one. Black, freshly assembled; red, fully discharged. XANES spectra of Fe_2O_3 , Fe_3O_4 , and FeO were also displayed for comparison. Pink, Fe_2O_3 ; blue, Fe_3O_4 ; green, FeO ; orange, Fe foil. Inset displays zoomed pre-edge region of: black, freshly assembled; red, fully discharged; pink, Fe_2O_3 ; blue, Fe_3O_4 . (b) Fe ion valence state vs their edge shifts (relative to Fe foil E_0) plot. (c) Ex situ Bi L_{III} -edge XANES spectra of the freshly assembled battery and fully discharged one. Black, freshly assembled; red, fully discharged; green, Bi_2O_3 ; blue, fully discharged state of the BiFeO_3 -Li battery.

located in tetrahedral sites. The pre-edge intensity of tetrahedrally coordinated metals could be very significant, such as the Mn K-edge of KMnO_4 ⁴² and the Cr K-edge of K_2CrO_4 ,⁴³ where Mn and Cr ions are located in tetrahedral sites. The edge position of the freshly assembled CeO_2 - $\text{Bi}_2\text{Fe}_4\text{O}_9$ -Li battery is similar to that of Fe_2O_3 and indicates that the valence state of Fe ions is +3. However, it indeed displayed a much more prominent pre-edge feature compared with Fe_2O_3 , which is consistent with its structure, where half of Fe ions are located in tetrahedral sites and connect two FeO_6 octahedrons along the *a* and *b* axis. After being fully discharged, the Fe K-edge shifted toward a lower-energy position and is consistent with the edge position of Fe_3O_4 . This indicates that during the discharge process Fe ions partly participated in charge transfer, and a fraction of Fe ions were reduced to +2. On the basis of valence states of Fe ions in standard compounds (FeO , Fe_3O_4 , and Fe_2O_3) and their E_0 shifts compared with that of Fe foil (Figure 5b), the Fe valence state in fully discharged $\text{Bi}_2\text{Fe}_4\text{O}_9$ can be directly calculated and is $\sim+2.75$ and indicates that 25% of Fe^{3+} ions were reduced to Fe^{2+} during the whole discharge process. It is also noted that the pre-edge feature of fully discharged compound still has a distinct intensity, indicating that the coordination environment of tetrahedral Fe ions is properly maintained.

3.3.2. Ex Situ $\text{Bi } L_{\text{III}}$ -Edge XANES Measurements. $\text{Bi } L_{\text{III}}$ -edge XANES spectra of the freshly assembled battery and fully discharged one were displayed in Figure 5c. Bi_2O_3 was also displayed in Figure 5c for comparison. For the L_{III} edge, the whiteline intensity is of great interest, which is the p-d transition and usually is an indicator of valence band vacancy information on the transition metals.^{44,45} The L_{III} -edge position of freshly assembled battery is very similar to that of Bi_2O_3 , and this indicates that Bi ions are also in the valence state of +3. For the fully discharged one, the Bi L_{III} -edge largely shifted toward lower-energy position, and the whiteline intensity also greatly decreased. The Bi L_{III} -edge XANES spectrum of the fully discharged BiFeO_3 was also displayed, and both the edge position and whiteline intensity are similar to that of discharged $\text{Bi}_2\text{Fe}_4\text{O}_9$. This indicates that Bi ions are reduced to Bi^0 during the discharge.^{19,20} However, both Fe ions and Bi ions are responsible for charge transfer in $\text{Bi}_2\text{Fe}_4\text{O}_9$, while in the case of BiFeO_3 , only Bi ions are responsible for charge transfer.^{19,20}

3.3.3. In Situ $\text{Bi } L_{\text{III}}$ -Edge XANES Measurements. The in situ $\text{Bi } L_{\text{III}}$ -edge XANES spectra were displayed in Figures 6a and 6b, where they were continuously collected, while the batteries are discharged using the spectro-electrochemical cell. (The spectrum obtained at 74.1 mAh/g is measured right after the in situ Fe K-edge measurement.) Before \sim 74.1 mAh/g, the Bi L_{III} -edge did not display any shifts and indicates that Bi ions are not responsible for charge transfer at this stage. Figure 6b displayed Bi L_{III} -edge XANES spectra when the battery is further discharged. Two features are mainly observed and are consistent with ex situ observations. The whiteline intensity of the Bi L_{III} -edge decreased, and the Bi L_{III} -edge continuously shifted toward the lower-energy position during the discharge. This is similar to what has been observed in the discharge of BiFeO_3 .^{19,20} The in situ Bi L_{III} -edge measurements indicate that Bi ions contribute to charge transfer in the second and third regions displayed in Figure 4a.

As observed from in situ Bi L_{III} -edge XANES, Bi ions are not responsible for charge transfer before 70 mAh/g (two-electron transfer). However, from ex situ Fe K-edge XANES, Fe ions contribute only one electron during the whole discharge

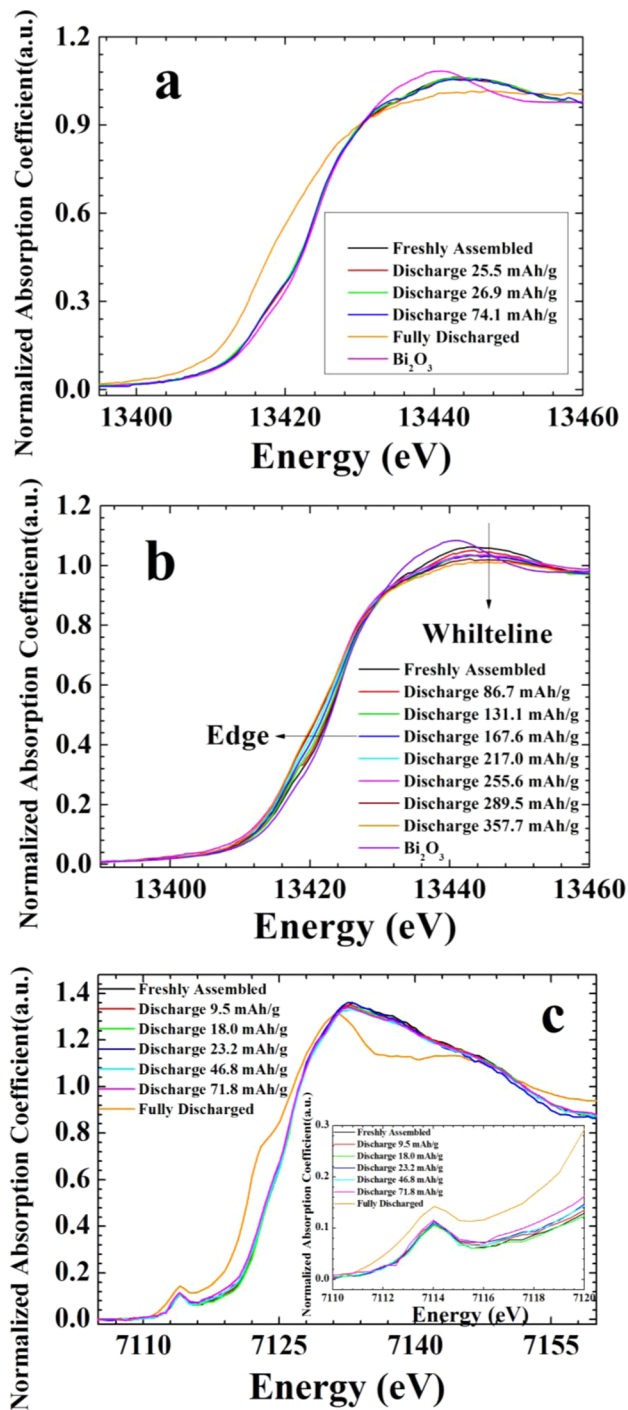


Figure 6. (a) In situ Bi L_{III} -edge XANES spectra collected during the discharge of the $\text{Bi}_2\text{Fe}_4\text{O}_9-\text{CeO}_2/\text{Li}$ battery using the spectro-electrochemical cell feature. Black, freshly assembled; red, discharged 25.5 mAh/g; green, discharged 26.9 mAh/g; blue, discharged 74.1 mAh/g; orange, fully discharged; pink, Bi_2O_3 . (b) Bi L_{III} -edge XANES spectra when the battery is further discharged. Black, freshly assembled; red, discharged 86.7 mAh/g; green, discharged 131.1 mAh/g; blue, discharged 167.6 mAh/g; light blue, discharged 217.0 mAh/g; pink, discharged 255.6 mAh/g; brown, discharged 289.5 mAh/g; orange, discharged 357.7 mAh/g; purple, Bi_2O_3 . (c) In situ Fe K-edge XANES spectra collected during the discharge process of the $\text{Bi}_2\text{Fe}_4\text{O}_9-\text{CeO}_2/\text{Li}$ battery using the spectro-electrochemical cell feature. Black, freshly assembled; red, discharged 9.5 mAh/g; green, discharged 18.0 mAh/g; blue, discharged 23.2 mAh/g; light blue, discharged 46.8 mAh/g; pink, discharged 71.8 mAh/g; orange, fully discharged. Inset displays an enlarged view of the Fe K-edge shifts.

process. To investigate whether Fe ions are responsible for charge transfer before 70 mAh/g, in situ Fe K-edge XANES measurements were performed.

3.3.4. In Situ Fe K-Edge XANES Measurements. In situ Fe K-edge XANES spectra were obtained while the battery was continuously discharged to ~ 71.8 mAh/g using a current density of ~ 5 mA/g and were displayed in Figure 6c. Over this period, the Fe K-edge was only slightly changed and did not show much shift compared with that of the fully discharged state. The edge shift did not display a systematic trend as well. This might indicate that Fe ions underwent a continuous reduction/oxidation during the Li ion insertion process.

Observed from in situ XANES measurements, neither Bi nor Fe ions were responsible for charge transfer before 70 mAh/g. Thus, oxygen ions may contribute to the discharge capacity. However, O^{2-} ions in the $\text{Bi}_2\text{Fe}_4\text{O}_9$ lattice cannot be reduced unless they were released from the $\text{Bi}_2\text{Fe}_4\text{O}_9$ lattice in the form of O_2 during the discharge process. To confirm this, in situ X-ray diffraction experiments were carried out.

3.4. Investigation of O_2 Release Using in Situ X-ray Diffraction. In situ X-ray diffraction patterns during the discharge process were collected and displayed in Figures 7a and b. Overall, diffraction peaks of $\text{Bi}_2\text{Fe}_4\text{O}_9$ not only display a

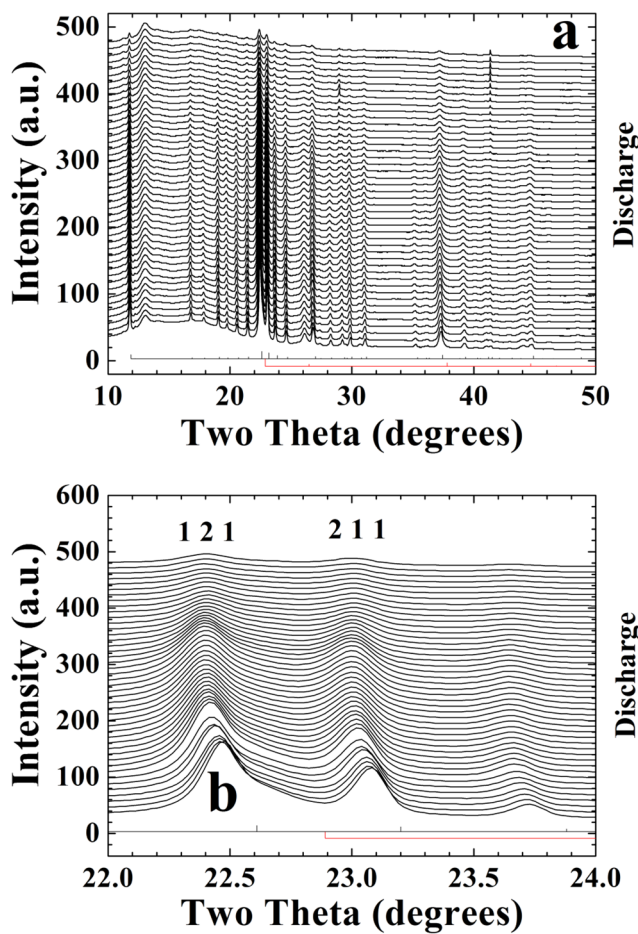


Figure 7. (a) In situ XRD patterns collected during the first discharge of the $\text{Bi}_2\text{Fe}_4\text{O}_9-\text{CeO}_2/\text{Li}$ battery using the spectro-electrochemical cell feature. (b) Zoomed view of the 2θ range between 22.0 and 24.0°. Diffraction patterns of standard $\text{Bi}_2\text{Fe}_4\text{O}_9$ (black) and CeO_2 (red) were displayed at the bottom. The electrochemical cycling profile for in situ measurements is displayed in Figure 9b.

significant shift at the beginning of discharge, but also the peak intensities display a significant decrease. This indicates that Li^+ ions were inserted into $\text{Bi}_2\text{Fe}_4\text{O}_9$. At the end of discharge, the diffraction peaks of $\text{Bi}_2\text{Fe}_4\text{O}_9$ can be barely observed. However, through the discharge process, no diffraction features of Bi^0 (or Li–Bi alloy) could be observed.^{18–20} This indicates that Bi^0/LiBi formed is in the nanoscale and is highly dispersed (or in an amorphous state).

Typical peak intensity changes of $\text{Bi}_2\text{Fe}_4\text{O}_9$ diffraction peaks (121), (001), and (211) were displayed in Figures 8a–c. As observed from Figure 8a, the peak intensity displays few inflection points in the discharge process. Figures 8b and c give a detailed view of this intensity change. According to the trend of intensity change, they can be divided into five regions and are separated at 35, 70, 140, and 210 mAh/g as highlighted in Figures 8b and c.

Before 35 mAh/g, which is about one-electron transfer, all diffraction peak intensities of (121), (001), and (211) display a similar feature of intensity change. First the diffraction peak intensity decreased before 16 mAh/g. After 16 mAh/g, the intensity increased. The peak intensity decreased again at ~20 mAh/g. After 28 mAh/g, the peak intensity increased again. These features of intensity change indicate that there is certain structural rearrangement in the ceramic lattice and are consistent with Figure 6c that Fe ions participate in the charge transfer during the first electron transfer process. While there are two kinds of Fe coordination environments in $\text{Bi}_2\text{Fe}_4\text{O}_9$, Fe^{3+} along the *a* and *b* axis is in the configuration of the tetrahedral coordination environment and is not stable upon reduction to Fe^{2+} ions, since high-spin Fe^{2+} ions are in d^6 configuration and are Jahn–Teller active. The Jahn–Teller effect of reduced Fe^{2+} rearranges the crystal structure and could affect the electrochemical contact between neighboring electrode materials and decrease the cell voltage. This is consistent with Figure 4b, where some batteries' discharge profiles also display similar features (twin peaks). The twin-peaks feature observed in Figures 8b and c might be a result of consequently Fe^{3+} reduction occurring along the *a* and *b* axis direction. Similar lattice distortions have also been reported for FeCr_2O_4 ⁴⁶ and $\text{Fe}_{1-x}\text{Zn}_x\text{V}_2\text{O}_4$,⁴⁷ where Fe^{2+} ions are in a high-spin tetrahedral coordination environment. During the oxygen reduction, tetrahedral Fe^{2+} ions should be reoxidized back to Fe^{3+} as observed from Figure 6c.

In region II, the peak intensity decreased linearly until 70 mAh/g, which is consistent with another one-electron transfer. A detailed view reveals that the trend of intensity change between 35 and 70 mAh/g (for the second electron transfer) displayed a different slope compared with that located between 70 and 140 mAh/g (region III). Octahedral Fe^{3+} ions along the *c* axis direction might participate in the charge transfer since there is no further structural rearrangement occurring.

In region III, the diffraction peak intensity decreased linearly until ~140 mAh/g, which is consistent with another two-electron transfer process. Correlating with Figure 6b, Bi^{3+} ions were continuously reduced to Bi^{2+} in this region ($2\text{Bi}^{3+}/$ formula). In region IV, the diffraction peak intensity decreased linearly until 210 mAh/g, which is consistent with another two-electron transfer process. Bi^{2+} ions were further reduced to Bi^{1+} . This indicates that Bi^{3+} ion reduction is through a three-step process, which has also been observed in the electrochemical discharge of BiFeO_3 .¹⁹ Since a full reduction of Bi^{3+} to Bi^0 in $\text{Bi}_2\text{Fe}_4\text{O}_9$ requires six-electron transfer, Bi ions were not fully reduced at 210 mAh/g. Above 210 mAh/g, the diffraction

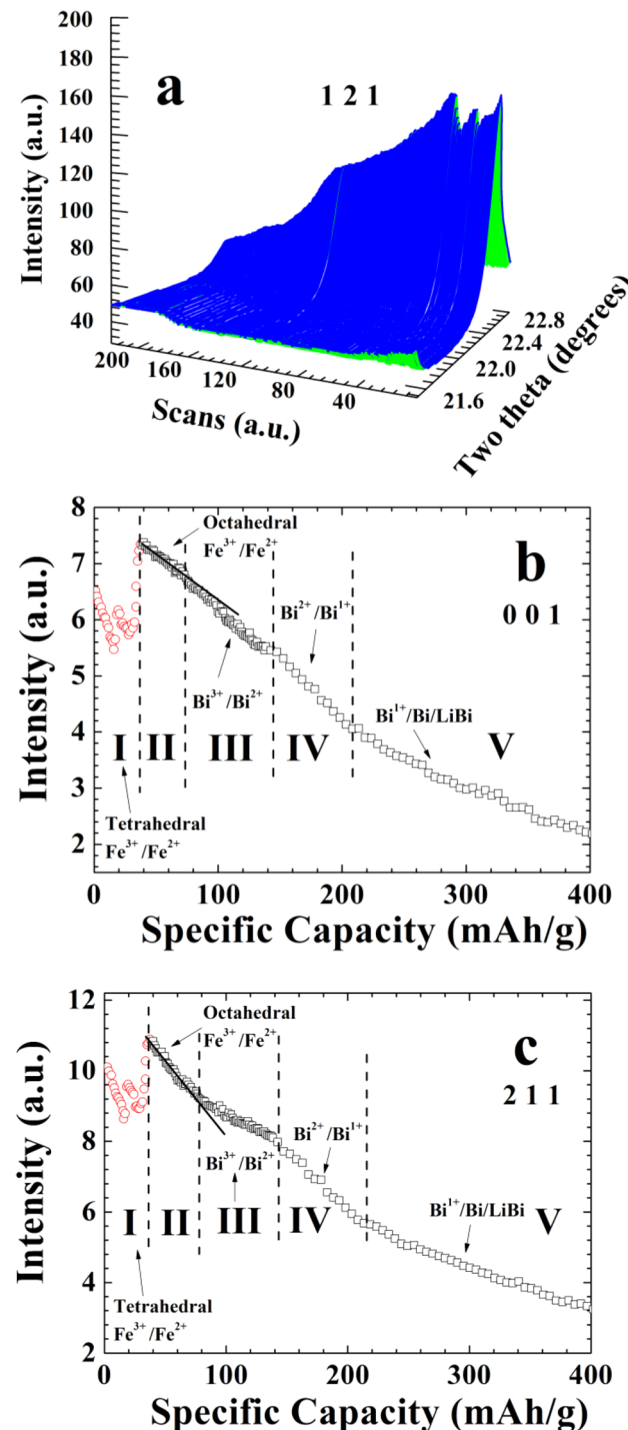


Figure 8. $\text{Bi}_2\text{Fe}_4\text{O}_9$ diffraction peak intensity change during the discharge of the $\text{Bi}_2\text{Fe}_4\text{O}_9$ –CeO₂/Li battery. (a) Three-dimensional plot of diffraction peak (121). The front and back sides of the diffraction peak are highlighted in blue and green, respectively. (b) Diffraction peak (001). (c) Diffraction peak (211).

intensity changes display a different trend again and indicate the further reduction of Bi^{1+} to Bi^0 followed by Li–Bi alloy formation.

Thus, Figure 8 actually can be closely correlated with Figure 4a, and the trend of diffraction peaks intensity change observed here can be used as an indicator for ionic species reduced in the ceramic matrix.

Figure 9a displays the percentage lattice parameter change during the discharge process. According to the trend of change, they can be divided into four regions and separated by 7, 18, 27, and 34 mAh/g. Overall, all lattice parameters of $\text{Bi}_2\text{Fe}_4\text{O}_9$ increased as the Li ions inserted into the ceramic lattice. Also, *a* and *b* axis lattice expansion are very similar and are slightly smaller compared with that of the *c* axis lattice. This indicates that Li ions are inserted into the $\text{Bi}_2\text{Fe}_4\text{O}_9$ lattice along the *a/b* plane direction and expand the crystal lattice isotropically. Compared with regions I and III, the $\text{Bi}_2\text{Fe}_4\text{O}_9$ lattice increased slightly slower in regions II and IV, as a result of the Jahn–Teller effect. This indicates that the crystal lattice underwent a slight shrinkage due to the Jahn–Teller distortion, which could decrease the electrochemical contact between the neighboring electrode materials. This slight shrinkage of the crystal lattice is the origin for the voltage dip displayed in insets of Figure 4b. Figure 9b displays the battery discharge profile while the in situ XRD patterns were collected.

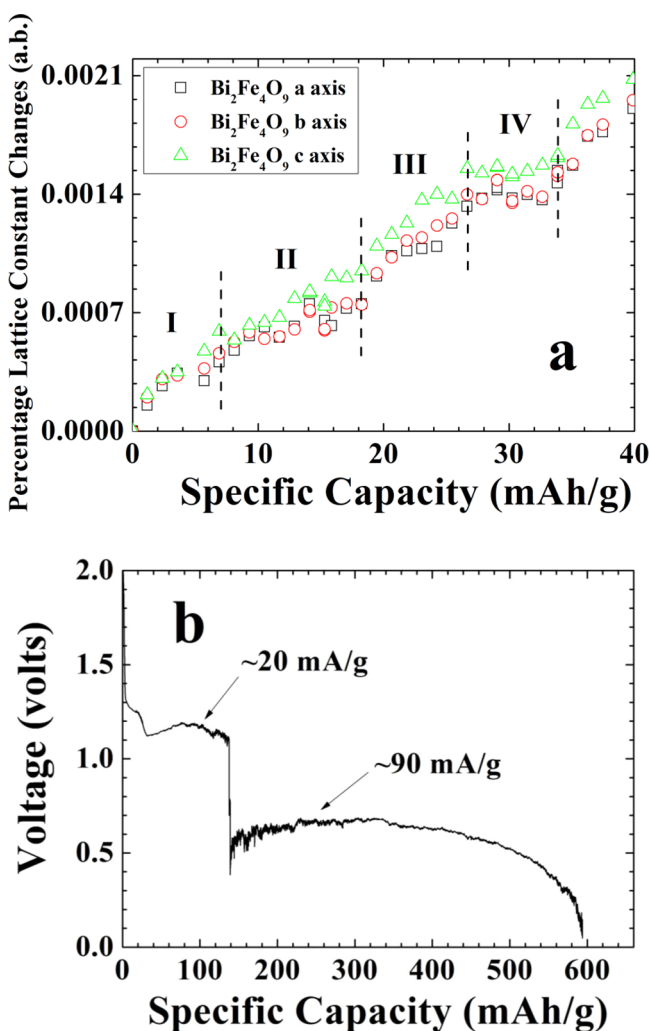


Figure 9. (a) $\text{Bi}_2\text{Fe}_4\text{O}_9$ percentage lattice constant changes of *a* axis, square; *b* axis, circle; *c* axis, triangle. (b) Electrochemical cycling profile for in situ measurements. Electrochemical discharge is carried out using two different current densities. Before ~ 140 mAh/g, it was discharged using a current density of ~ 20 mA/g to probe minor changes induced by Li^+ insertion. After that it was discharged with a current density of ~ 90 mA/g. This battery displays a discharge profile similar to that displayed in Figure 4a.

In some of the in situ XRD studies, the $\text{Bi}_2\text{Fe}_4\text{O}_9$ – CeO_2 –Li battery also displays a discharge profile similar to that observed in Figure 4b. Detailed profile fitting was performed (using XRD patterns at different discharge stages), and $\text{Bi}_2\text{Fe}_4\text{O}_9$ *a*, *b*, and *c* axes percentage lattice parameter changes are displayed in Figure 10a. Once the battery was discharged, $\text{Bi}_2\text{Fe}_4\text{O}_9$ *a* and *b*

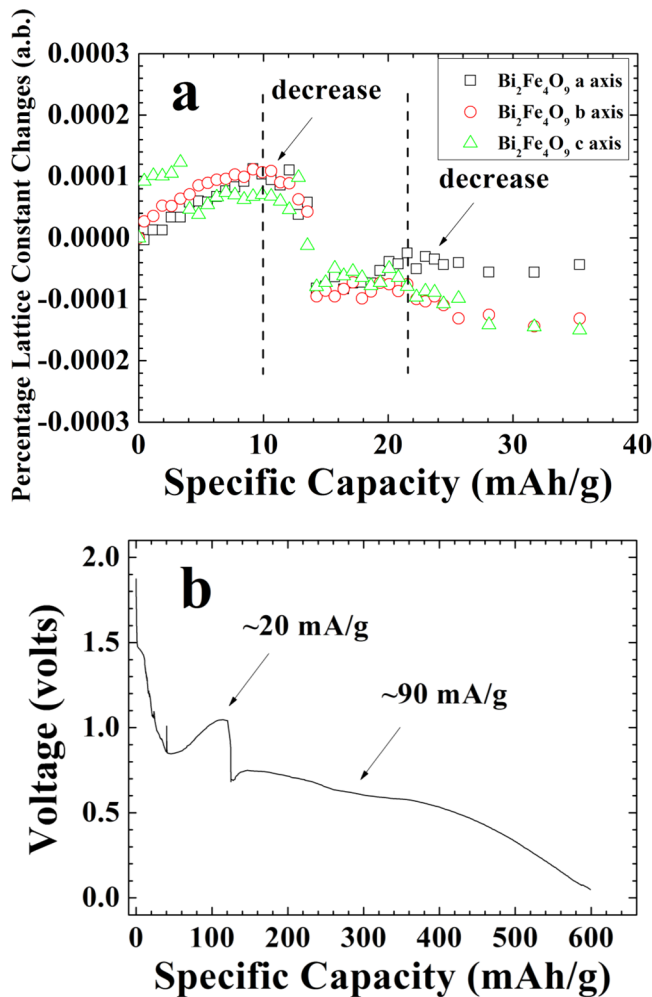


Figure 10. $\text{Bi}_2\text{Fe}_4\text{O}_9$ percentage lattice constant changes during in situ XRD studies. (a) *a* axis, square; *b* axis, circle; *c* axis, triangle. (b) Electrochemical cycling profile for the in situ measurements. Electrochemical discharge is carried out using two different current densities. Before ~ 120 mAh/g, it was discharged using a current density of ~ 20 mA/g to probe the minor changes induced by Li^+ insertion. After that it was discharged with a current density of ~ 90 mA/g. This battery displays a discharge profile similar to that displayed in Figure 4b (main figure).

lattice parameters were gradually increased, which indicates the intercalation of Li ions inside $\text{Bi}_2\text{Fe}_4\text{O}_9$. However, after a discharge capacity of ~ 10 mAh/g, the $\text{Bi}_2\text{Fe}_4\text{O}_9$ lattice largely decreased, and concomitantly, the cell voltage largely decreased as well (Figure 10b). The *c* axis changes followed a similar trend compared with those of *a* and *b* axes, except that it displays a sudden decrease at ~ 3 mAh/g. A detailed view of Figure 10a reveals that there is another lattice parameter decrease at ~ 22 mAh/g and is consistent with the in situ XRD analysis in Figures 8 and 9. Both Fe^{3+} ions along the *a* and *b* axis, which occupied the tetrahedral sites, could be slightly reduced before 35 mAh/g. The high-spin Fe^{2+} ions in

tetrahedral sites were not stable and caused the lattice shrinkage ~ 10 mAh/g, which decreased the electrochemical contact between neighboring $\text{Bi}_2\text{Fe}_4\text{O}_9-\text{CeO}_2$ particles, and the cell voltage decreased. Though the effect of Jahn–Teller distortion has also been observed in Figures 8 and 9, the lattice shrinkage observed in Figure 10a is much more significant and contributed to a voltage decrease to ~ 0.8 V. Figure 10b displays the battery discharge profile while the in situ XRD patterns were collected.

The percentage lattice parameter changes of CeO_2 during the discharge (the one used in Figure 10) are displayed in Figure 11a with the corresponding electrochemical discharge profile.

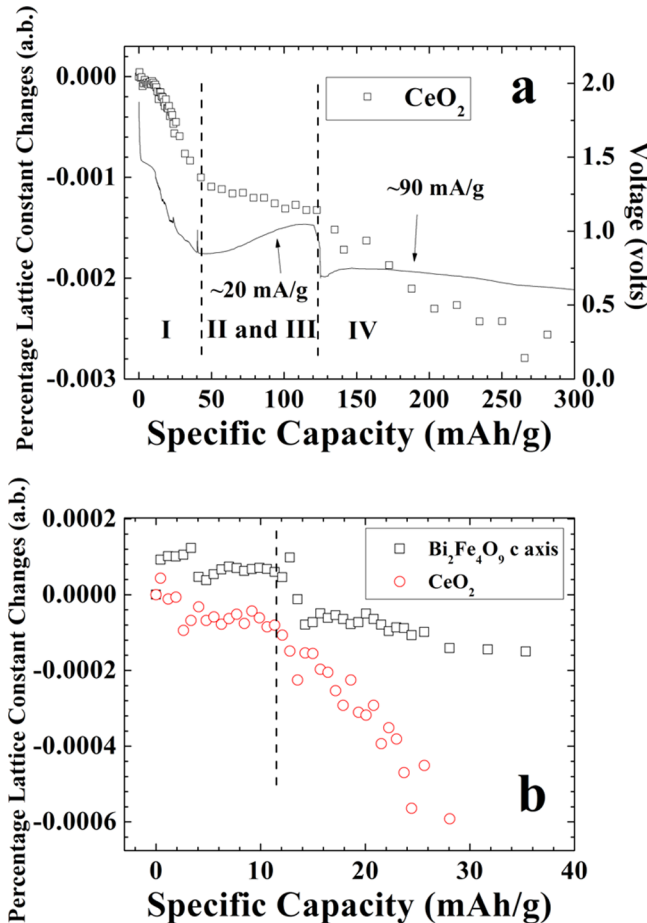


Figure 11. (a) CeO_2 percentage lattice constant changes during in situ XRD studies. Electrochemical cycling profile for in situ measurements is also displayed. The electrochemical discharge is carried out using two different current densities. Before ~ 120 mAh/g, it was discharged using a current density of ~ 20 mA/g to probe minor changes induced by Li^+ insertion. After that it was discharged with a current density of ~ 90 mA/g. (b) The percentage lattice constant changes of $\text{Bi}_2\text{Fe}_4\text{O}_9$, and CeO_2 during the in situ XRD studies. $\text{Bi}_2\text{Fe}_4\text{O}_9$ *c* axis, square; CeO_2 , circle.

At ~ 10 mAh/g, the CeO_2 lattice parameter also displays a decrease and indicates that there is certain charge transfer between CeO_2 and $\text{Bi}_2\text{Fe}_4\text{O}_9$ during the Li^+ insertion process. This is consistent with the TEM observations in Figure 3 that there can be significant oxygen vacancies at the interface of CeO_2 and $\text{Bi}_2\text{Fe}_4\text{O}_9$. As observed from Figure 11b, the onset of CeO_2 lattice parameter decrease occurred around the onset of Jahn–Teller distortion, indicating that shrinkage of the

$\text{Bi}_2\text{Fe}_4\text{O}_9$ crystal lattice is the origin for this charge transfer. The structural rearrangement induced by the Jahn–Teller distortion produced more oxygen vacancies in $\text{Bi}_2\text{Fe}_4\text{O}_9$, and part of the released O_2 was adapted by CeO_2 . A typical result of the intercalation of Li ions into ceramic lattice is the expansion of the crystal lattice, which is also true for intercalation of Li^+ into CeO_2 .⁴⁸ Thus, the lattice parameter decrease observed for CeO_2 is due to oxygen transportation from $\text{Bi}_2\text{Fe}_4\text{O}_9$ to CeO_2 .

CeO_2 is well-known to have oxygen storage capability and can release/adapt O_2 in a reducing/oxidation environment with concomitant increase/decrease of its lattice parameters.^{49–51} Thus, the lattice parameter change of CeO_2 could be used as an indicator for the direction of oxygen transportation. According to the slope of CeO_2 lattice parameter change, they could be divided into four regions. The first region is located before 35 mAh/g, where the CeO_2 lattice parameter changes vastly and the cell potential decreased to ~ 0.8 V. In this region, tetrahedral Fe^{3+} ions along the *a/b* plane (most probably the (002) crystal plane of $\text{Bi}_2\text{Fe}_4\text{O}_9$) participate in the charge transfer and release a large amount of O_2 . The second and third regions are located between 35 and ~ 120 mAh/g, where the ionic species along the *c* axis (Fe and Bi ions) participate in the charge transfer (regions II and III). At these regions, the CeO_2 lattice changes much slower compared with that in region I, and the cell potential increases. This also indicates that O_2 is continuously released out of the $\text{Bi}_2\text{Fe}_4\text{O}_9$ lattice when Fe or Bi ions were reduced. Region IV is located above 120 mAh/g, where the cell potential gradually decreased.

A detailed observation of the TEM images (Figure 12a) reveals that oxygen vacancies are largely formed in the $\text{Bi}_2\text{Fe}_4\text{O}_9$ (002) plane, while they can be barely observed in other crystal planes such as (201), (211), and (121). The (002) direction might be the direction for oxygen transfer. When CeO_2 adapted oxygen, its lattice parameter underwent an isotropic expansion along the *a*, *b*, and *c* lattices, which indicates that oxygen transportation is along its (111) plane, which is also consistent with TEM observation, where a significant amount of oxygen vacancies can be clearly observed (Figure 12b). However, as discussed in Figure 3, oxygen vacancies could also exist in the interface of $\text{Bi}_2\text{Fe}_4\text{O}_9$ (121) and CeO_2 (111), where those two have similar lattice spacing of 3.18 and 3.16 Å, respectively.

Certain metal oxides, such as TiO_2 ^{52,53} and CeO_2 ^{54,55} can easily release O_2 (produce oxygen vacancies) with reduction of certain cations for the charge balance.^{52,53} In $\text{Bi}_2\text{Fe}_4\text{O}_9-\text{CeO}_2$, there can also be this kind of phenomenon, and O_2 evolved out of the lattice participates in charge transfer in a way similar to what has been reported for a $\text{Li}-\text{O}_2$ battery, where continuous oxygen reduction to O^-/O^{2-} was proposed for the cathode reaction.^{56–58} As the O_2 gradually depleted in the discharge, the cell voltage decreased as well, and tetrahedral Fe^{3+} ions along the *a* and *b* plane were reduced, which invokes a structural rearrangement of the crystal and releases more O_2 . It is also noted that the (002) plane of $\text{Bi}_2\text{Fe}_4\text{O}_9$ is very reactive, where there are not only a lot of oxygen vacancies but also tetrahedral Fe^{3+} ions participating in producing more O_2 . During the oxygen reduction, tetrahedral Fe^{2+} ions were reoxidized back to Fe^{3+} . If this is the case, one can design an experiment to expose $\text{Bi}_2\text{Fe}_4\text{O}_9$ to the ambient, which can provide more O_2 , and the battery should discharge better.

3.5. O_2 Reduction Contributing to the Discharge. Two batteries were assembled and were discharged in two different ways. At different stages of the discharge process, the Mylar window was purposely cut a few small pinholes to expose

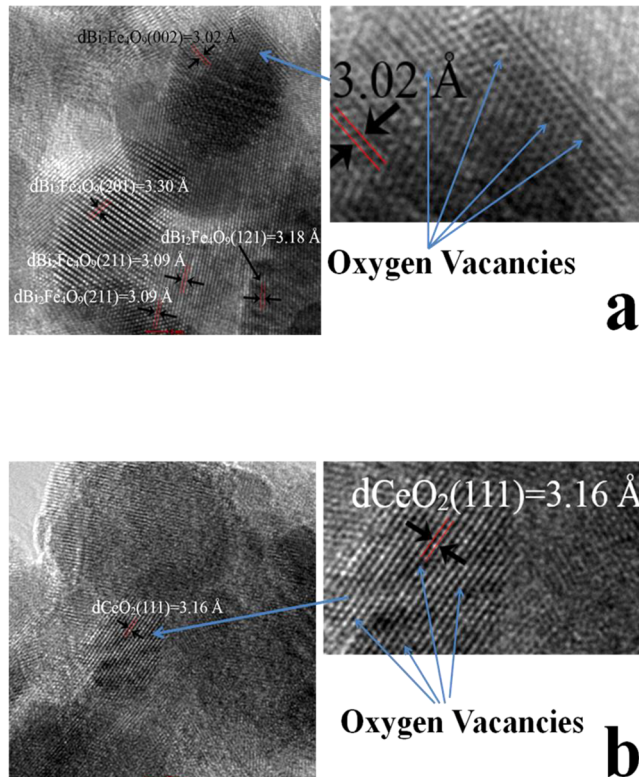


Figure 12. High-resolution TEM images of 30% Ce added $\text{Bi}_2\text{Fe}_4\text{O}_9$ (700°C). (a) $\text{Bi}_2\text{Fe}_4\text{O}_9$ (002), (201), (211), and (121) planes. Zoomed image is to highlight the oxygen vacancies in the (002) plane. (b) CeO_2 (111) plane. Zoomed image is to highlight the oxygen vacancies.

$\text{Bi}_2\text{Fe}_4\text{O}_9$ – CeO_2 to ambient environment. Battery I was discharged to ~ 48 mAh/g before it was exposed, and battery II was exposed to ambient from the beginning of discharge. Extra electrolyte was frequently added to always cover the pinholes during the discharge. As observed from Figure 13, these batteries displayed much better discharge voltage compared with that displayed in Figure 4a. When battery I was opened to ambient environment, it displays a large voltage increase of ~ 0.55 V at ~ 76 mAh/g. For battery II, which was opened to ambient from the beginning, a similar large voltage increase was observed at ~ 58 mAh/g with a voltage increase of ~ 0.57 V. This supports that O_2 is the origin for discharge capacity observed before 70 mAh/g. It was also observed that battery I did not display the voltage increase until it was opened to ambient for ~ 5.6 h. It seems like it will take some time for O_2 to dissolve and diffuse to the oxygen vacancies for the oxygen reduction reaction to occur. Similar oxygen transport properties have also been discussed in the literature, where an enhanced oxygen solubility and diffusion rate will increase the rate performance as well as discharge capacity.^{59–61}

4. CONCLUSION

CeO_2 -coated $\text{Bi}_2\text{Fe}_4\text{O}_9$ was successfully synthesized using a coprecipitation route, with 30% CeO_2 addition. Typical particle sizes of CeO_2 and $\text{Bi}_2\text{Fe}_4\text{O}_9$ are ~ 5 and 15 nm, respectively. A lot of oxygen vacancies existed in the CeO_2 (111) and $\text{Bi}_2\text{Fe}_4\text{O}_9$ (002) planes. At the interface of $\text{Bi}_2\text{Fe}_4\text{O}_9$ (121) and CeO_2 (111), where they have similar d -spacing, there are also oxygen vacancies existing. A discharge capacity of ~ 700 mAh/g can be obtained using two discharge current densities of ~ 90

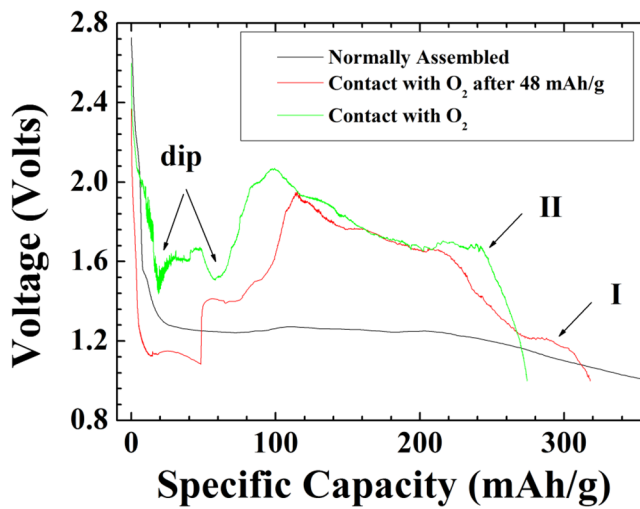


Figure 13. Galvanostatic cycling profiles of $\text{Bi}_2\text{Fe}_4\text{O}_9$ – CeO_2 /Li batteries using different discharge mode. Black: Normal discharge using a discharge current density of ~ 5 mA/g. Red: The battery is at first discharged to ~ 48 mAh/g at a current density of ~ 20 mA/g before the Mylar window ($\text{Bi}_2\text{Fe}_4\text{O}_9$ – CeO_2 side) had a few pinholes cut for exposure to ambient. The current density used after 48 mAh/g is ~ 5 mA/g. Green: The battery is discharged with a few pinholes at the Mylar window ($\text{Bi}_2\text{Fe}_4\text{O}_9$ – CeO_2 side) at a current density of ~ 5 mA/g.

and ~ 20 mA/g (with a cutoff voltage of 0.05 V). Oxygen reduction is responsible for the charge transfer, and $\text{Fe}^{3+}/\text{Fe}^{2+}$ redox couple participates in the discharge before 70 mAh/g. As soon as tetrahedral Fe^{3+} ions were reduced to Fe^{2+} , which is Jahn–Teller active, the $\text{Bi}_2\text{Fe}_4\text{O}_9$ crystal lattice shrank and decreased the cell voltage. In situ XRD studies further confirmed this, and its structural changes can be closely correlated with the electrochemical discharge voltage. The diffraction peak intensity change can also be used to identify the ionic species reduced during the electrochemical discharge process. Bi ions are responsible for the charge transfer between 70 and 210 mAh/g. After that, Bi^+ ions were further reduced to nano (or amorphous) Bi^0 followed by LiBi alloy formation. Fe K-edge and Bi L_{III}-edge XANES spectroscopy was employed to investigate the valence state change during the discharge process. Both Fe and Bi ions are responsible for the charge transfer during the Li intercalation process (with a cutoff voltage of 0.05 V). Jahn–Teller distortion of the tetrahedral high-spin Fe^{2+} induced a significant shrinkage of the $\text{Bi}_2\text{Fe}_4\text{O}_9$ lattice and largely decreased the cell voltage. Meanwhile, the onset of Jahn–Teller distortion enables the oxygen transfer between the interface of $\text{Bi}_2\text{Fe}_4\text{O}_9$ and CeO_2 and decreases CeO_2 lattice parameters. The (002) plane of $\text{Bi}_2\text{Fe}_4\text{O}_9$ is very reactive and not only produces significant oxygen vacancies but also has tetrahedral Fe^{3+} ions, which once reduced can shrink the $\text{Bi}_2\text{Fe}_4\text{O}_9$ lattice and further release more O_2 .

■ AUTHOR INFORMATION

Corresponding Author

*Tel.: +86 21 33933215. E-mail: wenwen@sinap.ac.cn.

Notes

The authors declare no competing financial interest.

ACKNOWLEDGMENTS

This work is supported by the National Basic Research Program of China (973 Program grants: 2010CB934501, 2010CB934503) and National Science Foundation of China (NSFC grants: 21203235, 21303147). The authors also thank beamlines BL14B1 and BL14W1 of SSRF (Shanghai Synchrotron Radiation Facility) for providing the beam time.

REFERENCES

- (1) Goodenough, J. B.; Park, K. S. The Li-Ion Rechargeable Battery: A Perspective. *J. Am. Chem. Soc.* **2013**, *135*, 1167–1176.
- (2) Rouxel, J. The Importance of Anions in Redox-Type Chimie Douce. *Mol. Cryst. Liq. Cryst.* **1998**, *310*, 1–4.
- (3) Rouxel, J. Anion–Cation Redox Competition and the Formation of New Compounds in Highly Covalent Systems. *Chem.—Eur. J.* **1996**, *2*, 1053–1059.
- (4) Wen, W.; Kumarasamy, B.; Mukerjee, S.; Auinat, M.; Ein-Eli, Y. Origin of 5 V Electrochemical Activity Observed in Non-Redox Reactive Divalent Cation Doped $\text{LiM}_{0.5+x}\text{Mn}_{1.5+x}\text{O}_4$ ($0 \leq x \leq 0.5$) Cathode Materials: In Situ XRD and XANES Spectroscopy Studies. *J. Electrochem. Soc.* **2005**, *9*, A1902.
- (5) Graetz, J.; Ahn, C. C.; Yazami, R.; Fultz, B. An Electron Energy-Loss Spectrometry Study of Charge Compensation in $\text{LiNi}_{0.8}\text{Co}_{0.2}\text{O}_2$. *J. Phys. Chem. B* **2003**, *107*, 2887–2891.
- (6) Ceder, G.; Chiang, Y.-M.; Sadoway, D. R.; Aydinol, M. K.; Jang, Y.-I.; Huang, B. Identification of Cathode Materials for Lithium Batteries Guided by First-Principles Calculations. *Nature* **1998**, *392*, 694–696.
- (7) Tsai, Y. W.; Hwang, B. J.; Ceder, G.; Sheu, H. S.; Liu, D. G.; Lee, J. F. In-Situ X-ray Absorption Spectroscopic Study on Variation of Electronic Transitions and Local Structure of $\text{LiNi}_{1/3}\text{Co}_{1/3}\text{Mn}_{1/3}\text{O}_2$ Cathode Material during Electrochemical Cycling. *Chem. Mater.* **2005**, *17*, 3191–3199.
- (8) Hu, S. K.; Cheng, G. H.; Cheng, M. Y.; Hwang, B. J.; Santhanam, R. Cycle Life Improvement of ZrO_2 -coated Spherical $\text{LiNi}_{1/3}\text{Co}_{1/3}\text{Mn}_{1/3}\text{O}_2$ Cathode Material for Lithium Ion Batteries. *J. Power Sources* **2009**, *188*, 564–569.
- (9) Chen, Z.; Dahn, J. R. Effect of a ZrO_2 Coating on the Structure and Electrochemistry of $\text{Li}_{x}\text{CoO}_2$ When Cycled to 4.5 V. *Electrochem. Solid-State Lett.* **2002**, *5*, A213–A216.
- (10) Ha, H. W.; Jeong, K. H.; Yun, N. J.; Hong, M. Z.; Kim, K. Effects of Surface Modification on the Cycling Stability of $\text{LiNi}_{0.8}\text{Co}_{0.2}\text{O}_2$ Electrodes by CeO_2 Coating. *Electrochim. Acta* **2005**, *50*, 3764–3769.
- (11) Wu, F.; Wang, M.; Su, Y. F.; Bao, L. Y.; Chen, S. Surface of $\text{LiCo}_{1/3}\text{Ni}_{1/3}\text{Mn}_{1/3}\text{O}_2$ Modified by CeO_2 -Coating. *Electrochim. Acta* **2009**, *54*, 6803–6807.
- (12) Koga, H.; Croguennec, L.; Ménétrier, M.; Douhil, K.; Belin, S.; Bourgeois, L.; Suard, E.; Weill, F.; Delmas, C. Reversible Oxygen Participation to the Redox Processes Revealed for $\text{Li}_{1.20}\text{Mn}_{0.54}\text{Co}_{0.13}\text{Ni}_{0.13}\text{O}_2$. *J. Electrochem. Soc.* **2013**, *160*, A786–A792.
- (13) Koga, H.; Croguennec, L.; Ménétrier, M.; Mannessiez, P.; Weill, F.; Delmas, C. Different Oxygen Redox Participation for Bulk and Surface: A Possible Global Explanation for the Cycling Mechanism of $\text{Li}_{1.20}\text{Mn}_{0.54}\text{Co}_{0.13}\text{Ni}_{0.13}\text{O}_2$. *J. Power Sources* **2013**, *236*, 250–258.
- (14) Sathiya, M.; Ramesha, K.; Rousse, G.; Foix, D.; Gonbeau, D.; Prakash, A. S.; Doublet, M. L.; Hemalatha, K.; Tarascon, J.-M. High Performance $\text{Li}_2\text{Ru}_{1-y}\text{Mn}_y\text{O}_3$ ($0.2 \leq y \leq 0.8$) Cathode Materials for Rechargeable Lithium-Ion Batteries: Their Understanding. *Chem. Mater.* **2013**, *25*, 1121–1131.
- (15) Sathiya, M.; Rousse, G.; Ramesha, K.; Laisa, C. P.; Vezin, H.; Sougrati, M. T.; Doublet, M.-L.; Foix, D.; Gonbeau, D.; Walker, W.; et al. Reversible Anionic Redox Chemistry in High-capacity Layered-Oxide Electrodes. *Nat. Mater.* **2013**, *12*, 827–835.
- (16) Amarilla, J. M.; Alonso, J. A.; Rojas, R. M. Structural Study of the Trigonal $\text{Bi}_{2.34}\text{U}_{0.33}\text{La}_{0.33}\text{O}_5$ Oxide Ion Conductor: Rietveld Refinement of X-ray and Neutron Powder Diffraction Data. *J. Chem. Soc., Dalton Trans.* **1999**, *7*, 1137–1141.
- (17) Kharton, V. V.; Naumovich, E. N.; Yaremchenko, A. A.; Marques, F. M. B. Research on the Electrochemistry of Oxygen Ion Conductors in the Former Soviet Union. *J. Solid State Electrochem.* **2001**, *5*, 160–187.
- (18) Xia, H.; Yan, F.; Lai, M. O.; Lu, L.; Song, W. D. Electrochemical Properties of BiFeO_3 Thin Films Prepared by Pulsed Laser Deposition. *Funct. Mater. Lett.* **2009**, *2*, 163–167.
- (19) Luo, S. H.; Gao, M.; Chen, J.; Xing, X. R.; Li, Z.; Zhou, X. T.; Wen, W. BiFeO_3 as Electrode Material for Lithium Batteries. *J. New Mater. Electrochem. Syst.* **2011**, *14*, 141–146.
- (20) Zhang, X. M.; Gao, M.; Gu, Y. L.; Bao, H. L.; Li, X. L.; Zhou, X. T.; Wen, W. The Structure–Property Investigation of $\text{Bi}_{1-x}\text{Ce}_x\text{FeO}_3$ ($x = 0, 0.05$)–Li Battery: In Situ XRD and XANES Studies. *J. Phys. Chem. C* **2012**, *116*, 20230–20238.
- (21) Bloom, I.; Hash, M. C.; Zebrowski, J. P.; Myles, K. M.; Krumpelt, M. Oxide-Ion Conductivity of Bismuth Aluminates. *Solid State Ionics* **1992**, *53–56*, 739–747.
- (22) Debnath, T.; Ruscher, C. H.; Fielitz, P.; Ohmann, S.; Borchardt, G. Series of Compositions $\text{Bi}_2(\text{M}'_x\text{M}_{1-x})_4\text{O}_9$ ($\text{M}' = \text{Al}, \text{Ga}, \text{Fe}; 0 \leq x \leq 1$) with Mullite-type Crystal Structure: Synthesis, Characterization and $^{18}\text{O}/^{16}\text{O}$ Exchange Experiment. *J. Solid State Chem.* **2010**, *183*, 2582–2588.
- (23) Kann, Z. R.; Auletta, J. T.; Hearn, E. W.; Weber, S. U.; Becker, K. D.; Schneider, H.; Lufaso, M. W. Mixed Crystal Formation and Structural Studies in the Mullite-type System $\text{Bi}_2\text{Fe}_4\text{O}_9$ – $\text{Bi}_2\text{Mn}_4\text{O}_{10}$. *J. Solid State Chem.* **2012**, *185*, 62–71.
- (24) Da Silva, K. L.; Šepelak, V.; Paesano, A., Jr.; Litterst, F. J.; Becker, H. D. Structural Studies of $\text{Bi}_2(\text{Fe}_x\text{Al}_{1-x})_4\text{O}_9$ Solid Solutions ($0.1 \leq x \leq 1.0$) Prepared by a Combined Mechanochemical/Thermal Synthesis. *Z. Anorg. Allg. Chem.* **2010**, *636*, 1018–1025.
- (25) Murshed, M. M.; Nenert, G.; Burianek, M.; Robben, L.; Muhlberg, M.; Schneider, H.; Fischer, R. X.; Gesing, T. M. Temperature-Dependent Structural Studies of Mullite-Type $\text{Bi}_2\text{Fe}_4\text{O}_9$. *J. Solid State Chem.* **2013**, *197*, 370–378.
- (26) Toby, B. H. CMPO-A Powder Diffraction Toolkit. *J. Appl. Crystallogr.* **2005**, *38*, 1040–1041.
- (27) Larson, A. C.; Von Dreele, R. B. GSAS General Structure Analysis System. Report LAUR 86–748, Los Alamos National Laboratory: Los Alamos, NM, 1995.
- (28) Rietveld, H. M. A Profile Refinement Method for Nuclear and Magnetic Structures. *J. Appl. Crystallogr.* **1969**, *2*, 65–71.
- (29) Toby, B. H. EXPGUI, A Graphical User Interface for GSAS. *J. Appl. Crystallogr.* **2001**, *34*, 210–213.
- (30) Lv, D. P.; Wen, W.; Huang, X. K.; Bai, J. Y.; Mi, J. X.; Wu, S. Q.; Yang, Y. A Novel $\text{Li}_2\text{FeSiO}_4/\text{C}$ Composite: Synthesis, Characterization and High Storage Capacity. *J. Mater. Chem.* **2011**, *21*, 9506–9512.
- (31) Zhong, K. F.; Zhang, B.; Luo, S. H.; Wen, W.; Li, H.; Huang, X. J.; Chen, L. Q. Investigation on Porous MnO Microsphere Anode for Lithium Ion Batteries. *J. Power Sources* **2011**, *196*, 6802–6808.
- (32) Lv, D. P.; Bai, J. Y.; Zhang, P.; Wu, S. Q.; Li, Y. X.; Wen, W.; Jiang, Z.; Mi, J. X.; Zhu, Z. Z.; Yang, Y. Understanding the High Capacity of $\text{Li}_2\text{FeSiO}_4$: In Situ XRD/XANES Study Combined with First-Principles Calculations. *Chem. Mater.* **2013**, *25*, 2014–2020.
- (33) Yoon, W. S.; Balasubramanian, M.; Chung, K. Y.; Yang, X. Q.; McBreen, J.; Grey, C. P.; Fischer, D. A. Investigation of the Charge Compensation Mechanism on the Electrochemically Li-Ion Deintercalated $\text{Li}_{1-x}\text{Co}_{1/3}\text{Ni}_{1/3}\text{Mn}_{1/3}\text{O}_2$ Electrode System by Combination of Soft and Hard X-ray Absorption Spectroscopy. *J. Am. Chem. Soc.* **2005**, *127*, 17479–17487.
- (34) Ein-Eli, Y.; Lu, S. H.; Rzeznik, M. A.; Mukerjee, S.; Yang, X. Q.; McBreen, J. $\text{LiCu}_x\text{Mn}_{2-x}\text{O}_4$ Spinels ($0.1 \leq x \leq 0.5$): A New Class of Cathode Materials for Li Batteries: II. In Situ Measurements. *J. Electrochem. Soc.* **1998**, *145*, 3383–3386.
- (35) Wang, Y. S.; Yu, X. Q.; Xu, S. Y.; Bai, J. M.; Xiao, R. J.; Hu, Y. S.; Li, H.; Yang, X. Q.; Chen, L. Q.; Huang, X. J. A Zero-strain Layered Metal Oxide as the Negative Electrode for Long-Life Sodium-Ion Batteries. *Nature Commun.* **2013**, *4*, 2365.

- (36) Ravel, B.; Newville, M. ATHENA, ARTEMIS, HEPHAESTUS: Data Analysis for X-ray Absorption Spectroscopy Using IFEFFIT. *J. Synchrotron Radiat.* **2005**, *12*, 537–541.
- (37) JCPDS card number: 340394.
- (38) Grugeon, S.; Laruelle, S.; Dupont, L.; Tarascon, J.-M. An Update on the Reactivity of Nanoparticles Co-based Compounds Towards Li. *Solid State Sci.* **2003**, *5*, 895–904.
- (39) Poizot, P.; Laruelle, S.; Grugeon, S.; Dupont, L.; Tarascon, J.-M. Nano-Sized Transition-Metal Oxides as Negative-Electrode Materials for Lithium-Ion Batteries. *Nature* **2000**, *407*, 496–499.
- (40) Gao, X. T.; Bare, S. R.; Weckhuysen, B. M.; Wachs, I. E. In Situ Spectroscopic Investigation of Molecular Structures of Highly Dispersed Vanadium Oxide on Silica under Various Conditions. *J. Phys. Chem. B* **1998**, *102*, 10842–10852.
- (41) Rodriguez, J. A.; Chaturvedi, S.; Hanson, J. C.; Albornoz, A.; Brito, J. L. Electronic Properties and Phase Transformations in CoMoO₄ and NiMoO₄: XANES and Time-Resolved Synchrotron XRD Studies. *J. Phys. Chem. B* **1998**, *102*, 1347–1355.
- (42) Gilbert, B.; Frazer, B. H.; Belz, A.; Conrad, P. G.; Nealson, K. H.; Haskel, D.; Lang, J. C.; Srager, G.; De Stasio, G. Multiple Scattering Calculations of Bonding and X-ray Absorption Spectroscopy of Manganese Oxides. *J. Phys. Chem. A* **2003**, *107*, 2839–2847.
- (43) Dubrail, J.; Farges, F. Not all Chromates Show the Same Pre-edge Feature. Implications for the Modelling of the Speciation of Cr in Environmental Systems. *J. Phys.: Conf. Ser.* **2009**, *190*, 012176.
- (44) Mukerjee, S.; Srinivasan, S.; Soriaga, M. P.; McBreen, J. Role of Structural and Electronic Properties of Pt and Pt Alloys on Electrocatalysis of Oxygen Reduction: An In Situ XANES and EXAFS Investigation. *J. Electrochem. Soc.* **1995**, *142*, 1409–1422.
- (45) Cuenya, B. R.; Croy, J. R.; Mostafa, S.; Behafarid, F.; Li, L.; Zhang, Z. F.; Yang, J. C.; Wang, Q.; Frenkel, A. I. Solving the Structure of Size-Selected Pt Nanocatalysts Synthesized by Inverse Micelle Encapsulation. *J. Am. Chem. Soc.* **2010**, *132*, 8747–8756.
- (46) Kyono, A.; Gramsch, S. A.; Yamanaka, T.; Ikuta, D.; Ahart, M.; Mysen, B. O.; Mao, H. K.; Hemley, R. J. The Influence of the Jahn-Teller Effect at Fe²⁺ on the Structure of Chromite at High Pressure. *Phys. Chem. Miner.* **2012**, *39*, 131–141.
- (47) Katsufuji, T.; Suzuki, T.; Takei, H.; Shingu, M.; Kato, K.; Osaka, K.; Takata, M.; Sagayama, H.; Arima, T. Structural and Magnetic Properties of Spinel FeV₂O₄ with Two Ions Having Orbital Degrees of Freedom. *J. Phys. Soc. Jpn.* **2008**, *77*, 053708.
- (48) Hua, C. X.; Fang, X. P.; Yang, Z. W.; Gao, Y. R.; Wang, Z. X.; Chen, L. Q. Lithium Storage Mechanism and Catalytic Behavior of CeO₂. *Electrochem. Commun.* **2012**, *25*, 66–69.
- (49) Wang, X.; Rodriguez, J. A.; Hanson, J. C.; Gamarra, D.; Martinez-Arias, A.; Fernandez-Garcia, M. In Situ Studies of the Active Sites for the Water Gas Shift Reaction over Cu–CeO₂ Catalysts: Complex Interaction between Metallic Copper and Oxygen Vacancies of Ceria. *J. Phys. Chem. B* **2006**, *110*, 428–434.
- (50) Barrio, L.; Estrella, M.; Zhou, G.; Wen, W.; Hanson, J. C.; Hungria, A. B.; Hornes, A.; Fernandez-Garcia, M.; Martinez-Arias, A.; Rodriguez, J. A. Unraveling the Active Site in Copper–Ceria Systems for the Water–Gas Shift Reaction: In Situ Characterization of an Inverse Powder CeO_{2-x}/CuO–Cu Catalyst. *J. Phys. Chem. C* **2010**, *114*, 3580–3587.
- (51) Han, W.; Wen, W.; Hanson, J. C.; Teng, X.; Marinkovic, N.; Rodriguez, J. A. One-Dimensional Ceria as Catalyst for the Low-Temperature Water–Gas Shift Reaction. *J. Phys. Chem. C* **2009**, *113*, 21949–21955.
- (52) Deskins, N. A.; Rousseau, R.; Dupuis, M. Defining the Role of Excess Electrons in the Surface Chemistry of TiO₂. *J. Phys. Chem. C* **2010**, *114*, 5891–5897.
- (53) Wendt, S.; Sprunger, P. T.; Lira, E.; Madsen, G. K. H.; Li, Z. S.; Hansen, J. O.; Matthiesen, J.; Blekinge-Rasmussen, A.; Laegsgaard, E.; Hammer, B.; Besenbacher, F. The Role of Interstitial Sites in the Ti3d Defect State in the Band Gap of Titania. *Science* **2008**, *320*, 1755–1759.
- (54) Rodriguez, J. A.; Ma, S.; Liu, P.; Hrbek, J.; Evans, J.; Pérez, M. Activity of CeO_x and TiO_x Nanoparticles Grown on Au(111) in the Water–Gas Shift Reaction. *Science* **2007**, *318*, 1757–1760.
- (55) Esch, F.; Fabris, S.; Zhou, L.; Montini, T.; Africh, C.; Fornasiero, P.; Comelli, G.; Rosei, R. Electron Localization Determines Defect Formation on Ceria Substrates. *Science* **2005**, *309*, 752–755.
- (56) Abraham, K. M.; Jiang, Z. A Polymer Electrolyte-Based Rechargeable Lithium/Oxygen Battery. *J. Electrochem. Soc.* **1996**, *143*, 1–5.
- (57) Lu, Y. C.; Xu, Z. C.; Gasteiger, H. A.; Chen, S.; Hamad-Schifferli, K.; Shao-Horn, Y. Platinum–Gold Nanoparticles: A Highly Active Bifunctional Electrocatalyst for Rechargeable Lithium–Air Batteries. *J. Am. Chem. Soc.* **2010**, *132*, 12170–12171.
- (58) Kraysberg, A.; Ein-Eli, Y. Review on Li–Air Batteries—Opportunities, Limitations and Perspective. *J. Power Sources* **2011**, *196*, 886–893.
- (59) Read, J.; Mutolo, K.; Ervin, M.; Behl, W.; Wolfenstein, J.; Driedger, A.; Foster, D. Oxygen Transport Properties of Organic Electrolytes and Performance of Lithium/Oxygen Battery. *J. Electrochem. Soc.* **2003**, *150*, A1351–A1356.
- (60) Sandhu, S. S.; Fellner, J. P.; Brutchen, G. W. Diffusion-Limited Model for a Lithium/Air Battery with an Organic Electrolyte. *J. Power Sources* **2007**, *164*, 365–371.
- (61) Laoire, C. O.; Mukerjee, S.; Abraham, K. M.; Plichta, E. J.; Hendrickson, M. A. Elucidating the Mechanism of Oxygen Reduction for Lithium–Air Battery Applications. *J. Phys. Chem. C* **2009**, *113*, 20127–20134.